

## Departures from Axisymmetric Balance Dynamics during Secondary Eyewall Formation

SERGIO F. ABARCA AND MICHAEL T. MONTGOMERY

*Naval Postgraduate School, Monterey, California*

(Manuscript received 7 February 2014, in final form 11 June 2014)

### ABSTRACT

Departures from axisymmetric balance dynamics are quantified during a case of secondary eyewall formation. The case occurred in a three-dimensional mesoscale convection-permitting numerical simulation of a tropical cyclone, integrated from an initial weak mesoscale vortex in an idealized quiescent environment. The simulation exhibits a canonical eyewall replacement cycle. Departures from balance dynamics are quantified by comparing the azimuthally averaged secondary circulation and corresponding tangential wind tendencies of the mesoscale integration with those diagnosed as the axisymmetric balanced response of a vortex subject to diabatic and tangential momentum forcing. Balance dynamics is defined here, following the tropical cyclone literature, as those processes that maintain a vortex in axisymmetric thermal wind balance.

The dynamical and thermodynamical fields needed to characterize the background vortex for the Sawyer-Eliassen inversion are obtained by azimuthally averaging the relevant quantities in the mesoscale integration and by computing their corresponding balanced fields. Substantial differences between azimuthal averages and their homologous balance-derived fields are found in the boundary layer. These differences illustrate the inappropriateness of the balance assumption in this region of the vortex (where the secondary eyewall tangential wind maximum emerges). Although the balance model does broadly capture the sense of the forced transverse (overturning) circulation, the balance model is shown to significantly underestimate the inflow in the boundary layer. This difference translates to unexpected qualitative differences in the tangential wind tendency. The main finding is that balance dynamics does not capture the tangential wind spinup during the simulated secondary eyewall formation event.

### 1. Introduction

A secondary eyewall of a tropical cyclone is a prominent coherent structure that is concentric to the primary eyewall and is characterized by maxima in convective activity and tangential winds. Secondary eyewalls are common in the most intense tropical cyclones (Hawkins and Helveston 2004, 2008; Kossin and Sitkowski 2009; Kuo et al. 2008). Secondary eyewalls have been found to be associated with intensity changes (Yang et al. 2013), including eyewall replacement cycles (Houze et al. 2007, and references therein), and with the longer duration of higher storm intensity (Kuo et al. 2008) and storm growth (Maclay et al. 2008). Despite the recognized importance of secondary eyewalls, there is, as of yet, no unified theory to explain secondary eyewall formation

(SEF) and to guide the development of forecast tools, which today tend to rely on empirical relations (Kossin and Sitkowski 2009).

A wide variety of physical processes aiming to explain SEF have been described. These include two-dimensional vortex interactions (Kuo et al. 2004, 2008), anisotropic upscale energy cascades (Terwey and Montgomery 2008), and changes in axisymmetric efficiency [as defined by Schubert and Hack (1982) and Hack and Schubert (1986)] related to the radial expansion of the azimuthally averaged tangential wind field and sustained latent heating outside of the primary eyewall (Rozoff et al. 2012). Other models propose wave-mean flow interaction associated primarily with vortex Rossby waves and their modification to the storm inner-core region (Montgomery and Kallenbach 1997; Martinez et al. 2010a,b; Menelaou et al. 2012; Qiu et al. 2010; Abarca and Corbosiero 2011) or the generation and accumulation of convectively induced potential vorticity anomalies and the absence of vortex Rossby wave activity (Judt and Chen 2010). Sun et al. (2013) proposed that SEF arises from a feedback

Corresponding author address: Sergio F. Abarca, Naval Postgraduate School, 589 Dyer Road, Root Hall, Room 254, Monterey, CA 93943.  
E-mail: sergio.abarca.fuente@gmail.com

Report Documentation Page		Form Approved OMB No. 0704-0188
<p>Public reporting burden for the collection of information is estimated to average 1 hour per response, including the time for reviewing instructions, searching existing data sources, gathering and maintaining the data needed, and completing and reviewing the collection of information. Send comments regarding this burden estimate or any other aspect of this collection of information, including suggestions for reducing this burden, to Washington Headquarters Services, Directorate for Information Operations and Reports, 1215 Jefferson Davis Highway, Suite 1204, Arlington VA 22202-4302. Respondents should be aware that notwithstanding any other provision of law, no person shall be subject to a penalty for failing to comply with a collection of information if it does not display a currently valid OMB control number.</p>		
1. REPORT DATE <b>OCT 2014</b>	2. REPORT TYPE	3. DATES COVERED <b>00-00-2014 to 00-00-2014</b>
4. TITLE AND SUBTITLE <b>Departures from Axisymmetric Balance Dynamics during Secondary Eyewall Formation</b>		5a. CONTRACT NUMBER
		5b. GRANT NUMBER
		5c. PROGRAM ELEMENT NUMBER
6. AUTHOR(S)		5d. PROJECT NUMBER
		5e. TASK NUMBER
		5f. WORK UNIT NUMBER
7. PERFORMING ORGANIZATION NAME(S) AND ADDRESS(ES) <b>Naval Postgraduate School, Department of Meteorology, Monterey, CA, 93943</b>		8. PERFORMING ORGANIZATION REPORT NUMBER
9. SPONSORING/MONITORING AGENCY NAME(S) AND ADDRESS(ES)		10. SPONSOR/MONITOR'S ACRONYM(S)
		11. SPONSOR/MONITOR'S REPORT NUMBER(S)
12. DISTRIBUTION/AVAILABILITY STATEMENT <b>Approved for public release; distribution unlimited</b>		
13. SUPPLEMENTARY NOTES		
14. ABSTRACT <b>Departures from axisymmetric balance dynamics are quantified during a case of secondary eyewall formation. The case occurred in a three-dimensional mesoscale convection-permitting numerical simulation of a tropical cyclone, integrated from an initial weak mesoscale vortex in an idealized quiescent environment. The simulation exhibits a canonical eyewall replacement cycle. Departures from balance dynamics are quantified by comparing the azimuthally averaged secondary circulation and corresponding tangential wind tendencies of the mesoscale integration with those diagnosed as the axisymmetric balanced response of a vortex subject to diabatic and tangential momentum forcing. Balance dynamics is defined here, following the tropical cyclone literature, as those processes that maintain a vortex in axisymmetric thermal wind balance. The dynamical and thermodynamical fields needed to characterize the background vortex for the Sawyer??? Eliassen inversion are obtained by azimuthally averaging the relevant quantities in the mesoscale integration and by computing their corresponding balanced fields. Substantial differences between azimuthal averages and their homologous balance-derived fields are found in the boundary layer. These differences illustrate the inappropriateness of the balance assumption in this region of the vortex (where the secondary eyewall tangential wind maximum emerges). Although the balance model does broadly capture the sense of the forced transverse (overturning) circulation, the balance model is shown to significantly underestimate the inflow in the boundary layer. This difference translates to unexpected qualitative differences in the tangential wind tendency. The main finding is that balance dynamics does not capture the tangential wind spinup during the simulated secondary eyewall formation event.</b>		
15. SUBJECT TERMS		

16. SECURITY CLASSIFICATION OF:			17. LIMITATION OF ABSTRACT <b>Same as Report (SAR)</b>	18. NUMBER OF PAGES <b>16</b>	19a. NAME OF RESPONSIBLE PERSON
a. REPORT <b>unclassified</b>	b. ABSTRACT <b>unclassified</b>	c. THIS PAGE <b>unclassified</b>			

Standard Form 298 (Rev. 8-98)  
Prescribed by ANSI Std Z39-18

between inward-moving rainbands, the balanced response to their source of heat, and unbalanced dynamics. [Wang et al. \(2013\)](#) proposed that a “net” radial force in the boundary layer is relevant in the process and [Qiu and Tan \(2013\)](#) emphasized the role of the asymmetric boundary layer. [Kepert \(2013\)](#) presented theoretical arguments, based mostly on linearized Ekman theory, to propose a feedback mechanism for secondary eye-wall formation that involves a local enhancement of the radial vorticity gradient, frictional updraft, and convection. The hypothesized feedback, based primarily on linear Ekman balance reasoning, has been falsified by [Montgomery et al. \(2014\)](#).

SEF has been proposed recently as an element of a new paradigm of tropical cyclone intensification ([Huang et al. 2012](#); [Abarca and Montgomery 2013](#)). As part of the new paradigm, [Smith et al. \(2009\)](#) showed that from the azimuthally averaged perspective, the spinup of the system-scale swirling circulation (i.e., the radial convergence of absolute angular momentum) occurs via two mechanisms. The first mechanism is physically rooted above the boundary layer, in the sense that it is the result of the radial gradient of buoyancy generation rate, associated with the aggregate latent heat release in deep convective clouds. This mechanism can be captured approximately by balance dynamics [as defined by [Shapiro and Willoughby \(1982\)](#)] and has been formulated in the context of the conservation of absolute angular momentum. The second spinup mechanism is physically rooted within the boundary layer and is the result of inward radial advection of absolute angular momentum (associated with frictional inflow) surpassing the depletion of absolute angular momentum by frictional torque. While this latter mechanism cannot operate without the first mechanism (through the coupling with the interior flow via the radial pressure gradient force), it is essentially a mechanism of the dynamics of the boundary layer and is manifested as a type of vortex breakdown. Accordingly, the boundary layer spinup mechanism lies outside the realm of balance dynamics. In this study, as in [Abarca and Montgomery \(2013\)](#), we follow [Smith et al. \(2009\)](#) and [Smith and Montgomery \(2010\)](#) in the adoption of a dynamical definition of the boundary layer. The term *boundary layer* will be used here to describe the shallow layer of strong inflow near the sea surface that arises largely because of the frictional disruption of balance dynamics near the surface (e.g., [Smith et al. 2009](#), their Fig. 6).

Scale analysis, high-resolution mesoscale integrations, and in situ observations of the hurricane ([Willoughby 1979](#); [Smith et al. 2009](#); [Möller and Shapiro 2002](#); [Zhang et al. 2001](#); [Willoughby 1990](#); [Bell and Montgomery 2008](#)) strongly suggest that on the vortex scale, a large

portion of the hurricane flow is in axisymmetric gradient and hydrostatic balance and consequently this part of the vortex should satisfy the thermal wind equation. To stay in such a balance state, a secondary circulation will develop to oppose the forcing of diabatic heating and/or friction. After the seminal work of [Eliassen \(1951\)](#), a number of authors (e.g., [Willoughby 1979](#); [Shapiro and Willoughby 1982](#)) have used the so-called Sawyer–Eliassen equation to diagnose the secondary circulation of a hurricane-like vortex forced by diabatic heating or momentum sources. The Sawyer–Eliassen equation has been used also as a mean-flow model in the limit of weak departures from circular flow, to study axisymmetric tropical cyclone intensification (e.g., [Bui et al. 2009](#)), tropical cyclone asymmetries (e.g., [Shapiro and Montgomery 1993](#); [Montgomery and Shapiro 1995](#); [Möller and Montgomery 2000](#); [Möller and Shapiro 2002](#)), the interaction of the tropical cyclone with its environment (e.g., [Challa and Pfeffer 1980](#); [Pfeffer and Challa 1981](#); [Persing et al. 2002](#); [Möller and Shapiro 2002](#)), and the extent to which vortex evolution during tropical cyclogenesis proceeds via axisymmetric balance dynamics ([Hendricks et al. 2004](#); [Montgomery et al. 2006](#); [Fang and Zhang 2011](#); [Wang 2012](#)).

As stated in the foregoing discussion, the azimuthally averaged flow associated with the first mechanism for system-scale spinup can be described approximately by balance dynamics. The more general conception of balance flow is a flow in which the velocity field is functionally related to the mass field (presumed to be related quasi-statically to the pressure field; [McIntyre 2012](#)). However, in this study, following the custom in tropical cyclone research, *axisymmetric balance flow* will be defined as that part of the hurricane primary circulation that satisfies the gradient and hydrostatic balance. We refer to *axisymmetric balance dynamics* as the axisymmetric processes that constrain the flow to remain in axisymmetric thermal wind balance. Here, the axisymmetric portion of the hurricane flow that does not satisfy the thermal wind equation is called *unbalanced flow* and the dynamics associated with unbalanced flow are referred to as *unbalanced dynamics*. Unlike many other studies, the concept of unbalance does not refer primarily to the effect of gravity waves. Instead, it includes the strong horizontal advective dynamics that arise because the momentum equations are coupled, on account of friction, in the region spanning the transition layer between the surface layer and the nearly inviscid vortex circulation in the bulk flow aloft.

It has been proposed that unbalanced dynamics, as defined herein, are an important element in SEF. Using a model–observation consistent dataset, [Wu et al. \(2012\)](#) and [Huang et al. \(2012\)](#) proposed that SEF is the

culmination of a sequence of structural changes of the mature tropical cyclone's inner core. These changes start with a radial expansion of the tangential wind field, followed by the response of the boundary layer, characterized by an increase in radial inflow and subsequently by the development of supergradient winds and an increase in horizontal convergence. [Abarca and Montgomery \(2013\)](#) presented a verification of this hypothesis using independent evidence from the idealized full-physics, high-resolution integration originally studied by [Terwey and Montgomery \(2008\)](#) and by [Terwey et al. \(2013\)](#) and with a slab boundary layer model. With this evidence, [Abarca and Montgomery \(2013\)](#) proposed that unbalanced dynamics are an important element for SEF. Alongside the model evidence, there is also in situ observational evidence that mature secondary eyewalls exhibit supergradient winds near the top of the boundary layer ([Didlake and Houze 2011](#); [Bell et al. 2012](#)).

In this study we will present a quantification of the degree to which SEF departs from balanced dynamics. It is based on the canonical SEF integration studied by [Terwey and Montgomery \(2008\)](#), [Terwey et al. \(2013\)](#), and [Abarca and Montgomery \(2013\)](#).

The manuscript is organized as follows: [section 2](#) describes the scientific methodology, the models, and their integrations; [section 3](#) presents the main results, and [section 4](#) provides a summary of the findings and concluding remarks. Two appendixes are included to address important methodological questions regarding the balance integrations and their robustness to the characterization of the background vortex.

## 2. Scientific methodology, models, and integrations

The methodology of this work consists essentially of comparing the results of two different flow model frameworks. One modeling framework is the Regional Atmospheric Modeling System (RAMS; [Pielke et al. 1992](#); [Cotton et al. 2002](#)). The other is the Sawyer–Eliassen equation and corresponding balanced tendency prediction as presented in [Bui et al. \(2009\)](#). We use azimuthal averages of the high-resolution model output of a canonical SEF event to integrate the Sawyer–Eliassen equation. A comparison of the secondary circulation and the derived tangential wind tendency of the two modeling frameworks is performed to quantify the extent to which the high-resolution, full-physics RAMS integration undergoing SEF is captured by axisymmetric balance dynamics. This procedure has been used previously to study the formation stage of incipient hurricane vortices (e.g., [Hendricks et al. 2004](#); [Montgomery et al. 2006](#); [Wang 2012](#)) and in mature hurricanes (e.g., [Bui et al. 2009](#); [Fudeyasu and Wang 2011](#)). The remainder

of this section summarizes the essential features of the two models and specific details of the methodology used to quantify departures from axisymmetric balance during SEF.

### a. The RAMS and the RAMS integration

RAMS is a three-dimensional nonhydrostatic numerical modeling system. For the purpose of the present study, we summarize the numerical integration, which exhibits a canonical SEF and eyewall replacement cycle, presented by [Terwey and Montgomery \(2008\)](#) and revisited by [Terwey et al. \(2013\)](#), [Abarca and Montgomery \(2013\)](#), and [Montgomery et al. \(2014\)](#). This simulation uses a surface flux parameterization based on the [Louis \(1979\)](#) scheme; the radiation scheme introduced by [Harrington \(1997\)](#); a subgrid-scale turbulence scheme based on [Smagorinsky \(1963\)](#), with the modifications from [Lilly \(1962\)](#) and [Hill \(1974\)](#); and the seven-species microphysical scheme by [Walko et al. \(1995\)](#), with the specification described in [Montgomery et al. \(2006\)](#).

The RAMS simulation used in this study is an idealized integration on an *f* plane ( $15^{\circ}\text{N}$ ) with a constant sea surface temperature of  $28^{\circ}\text{C}$ . The model is configured with 30 vertical levels (vertical grid spacing varies from 300 m near the surface to 1800 m near the top of the domain, at about 26-km altitude). The model configuration has a parent domain, and two (two-way interactive) nested domains. Each nested domain is located at the center of the parent grid. Horizontal grid spacing is 24, 6, and 2 km; and there are 168, 170, and 251 grid points respectively. The outermost grid is cyclic in the horizontal direction. The initial condition is characterized by a quiescent environment [[Jordan's \(1958\)](#) sounding]. It contains a weak ( $10 \text{ m s}^{-1}$ ) mesoscale cyclonic vortex, located at the center of the three domains (with maximum speed at 4-km height and 75-km radius), that is initially in thermal wind balance. A positive moisture anomaly (water vapor mixing ratio increased up to  $1.3 \text{ g kg}^{-1}$  near the center of the initial vortex) is specified also. Further details of the RAMS experimental setup can be found in [Terwey and Montgomery \(2008\)](#), [Montgomery et al. \(2006\)](#), [Terwey et al. \(2013\)](#), and [Abarca and Montgomery \(2013\)](#). In this study we present azimuthal and 1-h time averages of the simulated variables. Such averages are obtained after interpolating the RAMS data from its original Arakawa C grid in Cartesian coordinates into a cylindrical grid (the center is determined as the centroid of the potential vorticity field in the lowest 7.3 km of the domain).

### b. The Sawyer–Eliassen model

The Sawyer–Eliassen equation is a diagnostic equation for the meridional streamfunction in the radius–height plane. This equation determines the meridional circulation

required to maintain a vortex, under heat and momentum forcing, in hydrostatic and gradient wind balance. There are several derivations of the Sawyer–Eliassen equation in the literature (e.g., [Shapiro and Willoughby 1982](#); [Schubert et al. 2007](#)). In this study we integrate the version derived by [Bui et al. \(2009\)](#):

$$\begin{aligned} \frac{\partial}{\partial r} \left[ -g \frac{\partial \chi}{\partial z} \frac{1}{\rho r} \frac{\partial \psi}{\partial r} - \frac{\partial}{\partial z} (\chi C) \frac{1}{\rho r} \frac{\partial \psi}{\partial z} \right] \\ + \frac{\partial}{\partial z} \left\{ \left[ \xi \chi (\xi + f) + C \frac{\partial \chi}{\partial r} \right] \frac{1}{\rho r} \frac{\partial \psi}{\partial z} - \frac{\partial}{\partial z} (\chi C) \frac{1}{\rho r} \frac{\partial \psi}{\partial r} \right\} \\ = g \frac{\partial}{\partial r} (\chi^2 Q) + \frac{\partial}{\partial z} (C \chi^2 Q) - \frac{\partial}{\partial z} (\chi \xi F_\lambda). \end{aligned} \quad (1)$$

Here  $g$  represents the acceleration due to gravity ( $9.81 \text{ m s}^{-2}$ ),  $f$  is the Coriolis parameter (evaluated here at  $15^\circ\text{N}$ , as in the RAMS simulation),  $\rho$  is the air density,  $r$  is the radius, and  $z$  is the physical height above sea level. Also,  $\chi = 1/\theta$ , where  $\theta$  is the potential temperature,  $\xi = (1/r)(\partial v/\partial r)$  is the vertical relative vorticity for the mean vortex ( $v$  is the tangential wind velocity),  $C = (v^2/r) + fv$  is the compound Coriolis and centrifugal force per unit mass, and  $\xi = (2v/r) + f$  is the modified Coriolis parameter. The transverse streamfunction  $\psi$  is defined such that the radial and vertical wind velocities  $u$  and  $w$ , respectively, are  $u = -(1/r)(\partial \psi / \partial z)$  and  $w = (1/r)(\partial \psi / \partial r)$  [see [Bui et al. \(2009\)](#) for details]. Finally,  $Q$  and  $F_\lambda$  are the forcing functions, representing the diabatic heating and tangential momentum sources, respectively. These last two functions are defined explicitly below, in [section 2c\(2\)](#), along with details of the integration of Eq. (1).

### c. The Sawyer–Eliassen integrations

To characterize the balanced vortex and the forcing functions used to integrate the balance model, we use RAMS azimuthal and 1-h averaged fields centered at hour 174 (when the simulation was undergoing SEF; see [section 3](#) for details of the secondary eyewall in the mesoscale model). In this section we describe how we integrate the Sawyer–Eliassen model, using the RAMS integration. We describe also aspects regarding the ellipticity condition in the Sawyer–Eliassen integrations.

#### 1) BALANCED VORTEX

The vortex used to integrate the balance model is constructed here in two different ways (and other ways in [appendix B](#)). First, we follow [Smith \(2006\)](#) and use the RAMS azimuthally averaged and time-averaged tangential wind field to compute its corresponding balanced density field. In this procedure, to initialize the density integration, we use the vertical density profile from the RAMS model at large radius. This methodology uses the

thermal wind equation, as well as the equation of state to calculate, without approximation, the thermodynamical fields necessary to integrate Eq. (1).

The second method of constructing the balanced vortex is to use the azimuthally averaged pressure and density fields from the RAMS model output to infer the corresponding balanced tangential wind field. In this method we follow the definition of gradient wind flow in [Holton \(2004\)](#). As pointed out in [Bui et al. \(2009\)](#), for a given mass field, it is not always possible to calculate the corresponding balanced tangential wind field. This computation requires the solution of a quadratic formula in which the radicand can become negative. In the data used in this work, the radicand becomes negative only in some sparse regions of the outflow layer and the problem is avoided locally by setting  $\partial p / \partial r = 0$  when the quantity becomes positive.

At this point, it is useful to recall that azimuthally averaged thermodynamical and dynamical fields from mature hurricane mesoscale integrations are not generally in axisymmetric balance with each other. However, it has been a common practice to integrate the Sawyer–Eliassen model with such azimuthal averages (e.g., [Hendricks et al. 2004](#); [Montgomery et al. 2006](#); [Fang and Zhang 2011](#); [Wang 2012](#)). In [appendix B](#) we present an integration of the Sawyer–Eliassen model characterizing the vortex with azimuthally averaged fields from the RAMS integration. It will be shown here that the conclusions obtained using the strict balance definitions of [Smith \(2006\)](#) and [Holton \(2004\)](#) or azimuthal averages are qualitatively consistent with each other so that the general conclusions of this manuscript are robust to any of these methodologies.<sup>1</sup>

#### 2) FORCING FUNCTIONS

The Sawyer–Eliassen model is integrated with diabatic heating and momentum forcing diagnosed from azimuthal and time averages of the RAMS integrations. Following [Bui et al. \(2009\)](#), the azimuthally averaged and time-averaged diabatic forcing  $Q$  is computed as the difference between the total diabatic heating rate and eddy heat fluxes, ignoring subgrid-scale heat diffusion, as

$$Q = \bar{\theta} - \overline{u' \frac{\partial \theta'}{\partial r}} - \frac{\bar{v'} \frac{\partial \theta'}{\partial \lambda}}{r} - \overline{w' \frac{\partial \theta'}{\partial z}}. \quad (2)$$

<sup>1</sup> Although it should be clear from the findings summarized herein, we point out that the robustness of our findings should not be construed to mean that the azimuthally averaged fields are in thermal wind balance. This is indeed not the case, as the differences displayed in [Figs. 2](#) and [3](#) attest. See upcoming discussion for further details.

Here the overbar denotes azimuthal average on a constant height surface and the prime denotes deviations therefrom;  $\dot{\theta}$  represents the azimuthally averaged total diabatic heating rate. Other symbols are as defined previously.

The azimuthally averaged and time-averaged tangential momentum source  $F$  is computed as the difference between the local time change of tangential momentum and the sum of the mean absolute vorticity flux and the mean vertical advection:

$$F_\lambda = \frac{\partial \bar{v}}{\partial t} + \bar{u}(\bar{\zeta} + f) + \bar{w} \frac{\partial \bar{v}}{\partial z}. \quad (3)$$

The forcing functions obtained for both momentum and heat are spatially coherent (see section 3b) and qualitatively consistent with similar diagnostics presented in other work (e.g., Bui et al. 2009, their Fig. 3).

### 3) OTHER ASPECTS, BOUNDARY CONDITIONS, AND REGULARIZATION

To integrate the Sawyer–Eliassen model, Eq. (1) is approximated with finite differences, as in Bui et al. (2009). The radial and vertical grid spacing is 2 km and 500 m, respectively.<sup>2</sup> A computational domain of 222-km radius and 15-km height is used. Equation (1) is solved numerically using the successive overrelaxation scheme (SOR) described in Press et al. (1992). An overrelaxation parameter of 1.8 is used and the solution is considered converged when the absolute error of the discrete equivalent of Eq. (1) is less than the prescribed value of  $10^{-24}$  (which is typically 10 orders of magnitude smaller than the magnitude of the forcing).

The boundary conditions of Eq. (1) at the axis of rotation and at the upper and lower boundaries are chosen as  $\psi = 0$  (i.e., the normal velocity is equal to zero). The normal velocity at the outer radius (inflow) is important to the conclusions of this study and therefore is not prescribed (setting it to zero or to the inflow value from the RAMS integration would artificially constrain the solution). Instead, the boundary condition at the outer radius is taken as  $\partial\psi/\partial r = 0$  (i.e., with the vertical velocity equal to zero).

Equation (1) is an elliptic partial differential equation given that the discriminant

$$D = \left[ \frac{\partial}{\partial z} (\chi C) \right]^2 + g \frac{\partial \chi}{\partial z} \left[ \xi \chi (\zeta + f) + C \frac{\partial \chi}{\partial r} \right] \quad (4)$$

<sup>2</sup>A vertical grid spacing of 300 m was also considered (not shown). The higher-resolution integrations rendered solutions with some small quantitative differences with respect to the solutions shown below. However, none of these differences altered in any way the conclusions of this manuscript.

is negative (note that the second term on the right-hand side is typically negative because it is proportional to  $\partial\chi/\partial z$ ). At some grid points, the balanced vortices described in section 1 (and the nonbalanced vortex described in appendix A) do not satisfy the ellipticity condition. The ellipticity condition can be violated when  $\partial(\chi C)/\partial z$  is too large, when  $[\xi \chi (\zeta + f) + C \partial \chi / \partial r]$  becomes negative, or when  $\partial \chi / \partial z$  becomes positive. To avoid violation of the ellipticity condition, a regularization procedure is implemented, following Möller and Shapiro (2002) and Bui et al. (2009).

As discussed in Möller and Shapiro (2002) and in Bui et al. (2009), the application of a regularization procedure makes modifications to the stability parameters so a convergent solution is obtained without changing the basic vortex structure. The regularization procedure is as follows: In those points where the ellipticity condition is violated, the regularization procedure reduces the term  $\partial(\chi C)/\partial z$  to 0.15 of its value. Then it evaluates  $[\xi \chi (\zeta + f) + C \partial \chi / \partial r]$  at every grid point. If any of the latter values is negative, the magnitude of the smallest value is multiplied by  $-1.1$  and added to all grid points. Finally, for the balanced calculations that result in negative vertical gradients of potential temperature near the top of the boundary layer (see discussion below), at those grid points where  $\partial \chi / \partial z$  is positive (regions of dry, static vertical instability), the procedure recalculates the value of potential temperature by assuming  $\partial \theta / \partial z = 2 \text{ K km}^{-1}$ . The same adjustment is applied to the grid points above the grid point where the ellipticity condition is violated, up to the height where the adjusted potential temperature is less than that of the original vortex. This vertical extension of the modification avoids sharp gradients of potential temperature. As an example, at 80-km radius, this procedure modifies the temperature structure within the layer between 1.5- and 4.5-km heights. We note that changing the order of the three criteria applied does not change any of the results presented. We note also that changing the term  $\partial(\chi C)/\partial z$  to fractions larger than 0.15 of its value (e.g., 0.4, 0.6, or 0.8) results in local violation of the ellipticity criteria, but with a solution that still converges and renders a secondary circulation practically indistinguishable from those considered here.

## 3. Results

### a. Secondary eyewall formation in the RAMS integration

We begin this section by reviewing the main evidence of SEF in the RAMS integration. Then we introduce the

azimuthally averaged fields from the RAMS integration and the corresponding calculated balanced fields used to integrate the Sawyer–Eliassen model. We describe also details of the Sawyer–Eliassen integrations and conclude with a discussion of departures from balance dynamics during SEF, as summarized in the introduction.

The synthetic storm in the RAMS integration evolves from a weak mesoscale convective vortex to a mature hurricane that undergoes a canonical eyewall replacement cycle. Terwey and Montgomery (2008), Terwey et al. (2013), Abarca and Montgomery (2013), and Montgomery et al. (2014) have discussed the SEF kinematics and basic dynamics of the simulation. The time series of minimum pressure, radius of maximum winds (at about 150-m height), and maximum azimuthal-mean tangential winds (at 1-km height) for the 220-h numerical simulation are presented in Terwey and Montgomery (2008, their Fig. 2). The characteristic tangential wind increase in the SEF radial region along with the decrease in the tangential wind of the primary eyewall is captured in the figure as the sudden expansion of the radius of maximum winds (from 35- to 80-km radius, just before hour 180). The main characteristics of the azimuthally averaged tangential wind evolution and vertical velocity are presented also in radius–time diagrams in Terwey et al. (2013, their Fig. 1) and in Abarca and Montgomery (2013, their Fig. 1). These diagrams show that the simulated eyewall replacement cycle is fully consistent with observations of the phenomena (e.g., Willoughby et al. 1982; Houze et al. 2007; Bell et al. 2012; Sitkowski et al. 2012) and with other realistic numerical integrations (e.g., Abarca and Corbosiero 2011; Zhou and Wang 2011; Zhou et al. 2011).

Figure 1 shows the radius–height structure of azimuthally averaged tangential wind velocity and secondary circulation at select times during the RAMS integration, within 200 km of the system-scale circulation center. The top row corresponds to hour 72, when the vortex was intensifying with a single eyewall, and the remaining rows (hours 174, 179, 183, and 189) present the vortex with an emerging and evolving secondary eyewall.

Figure 1 shows also that the RAMS integration exhibits the typical tangential wind structure and secondary circulation of single-eye hurricanes and a structure fully consistent with the in situ observations of hurricanes with double eyewalls (e.g., Houze et al. 2007, their Fig. 2, and Bell et al. 2012, their Figs. 6 and 8). Figure 1 is similar to Abarca and Montgomery (2013), but instead of employing 2-h averages, we show 1-h averaged fields, as a simple way to limit the impact of time averaging the evolving flow during the diagnosis time. The right panels allow for a more direct comparison with observational

results (Bell et al. 2012, their Figs. 6 and 8). As emphasized by Abarca and Montgomery (2013), the secondary tangential wind maximum emerges near the top, but within the boundary layer.<sup>3</sup> We note that the secondary wind maximum emerges in a vertically confined region, with the vertical elongation of the  $60 \text{ m s}^{-1}$  isotach in Fig. 1c spanning only about 500 m in height. Such a narrow vertical region with large tangential winds evolves to occupy a broader vertical extent, of about 2 km at hour 183 and about 2.5 km at hour 189 (Figs. 1e,g).

As noted in Abarca and Montgomery (2013), Fig. 1 shows also a much broader tangential wind field during SEF (Fig. 1c) than during the single-eyewall phase of storm intensification (Fig. 1a). Abarca and Montgomery (2013) showed that this structure change is a progressive one (see their Fig. 1a), consistent with the ideas presented by Huang et al. (2012, their Figs. 1c–f) and Wu et al. (2012, their Fig. 6a). Finally, the figure shows how the forming secondary eyewall is characterized by a broad radial region of ascending motion (Fig. 1d) that becomes radially narrower with time (Figs. 1f,h) as the secondary eyewall forms. This progressive radial focusing of the azimuthally averaged upward motion is also visible in Fig. 1b of Abarca and Montgomery (2013) and seems to be a characteristic signature of SEF.

### b. Balanced temperature and wind fields

We now present and discuss balanced fields calculated from azimuthally averaged and time-averaged RAMS fields, as captured during SEF. As a representative time, we show the results centered at hour 174. However, the described processes are consistent with findings from other analysis times (e.g., hours 162, 166, 170; not shown). Figure 2 shows the azimuthally averaged tangential wind field at 174 h (as in Fig. 1c) and its corresponding balanced potential temperature field. The latter is calculated following (Smith 2006), as detailed in section 2c(1), using the tangential wind field in Fig. 2a. As expected from the thermal wind equation, the balanced potential temperature field exhibits a warm-core structure in most of the troposphere, above the height of maximum winds. It shows also a cold-core structure at very low levels, in the boundary layer, in the region where tangential winds increase with height.

In the balanced field, the near-surface potential temperature at around 30-km radius (below the location of the wind maximum) reaches a value lower than  $-30^\circ\text{C}$ . The unrealistic cold anomaly was observed also

<sup>3</sup>See the introduction for our working definition for the boundary layer.

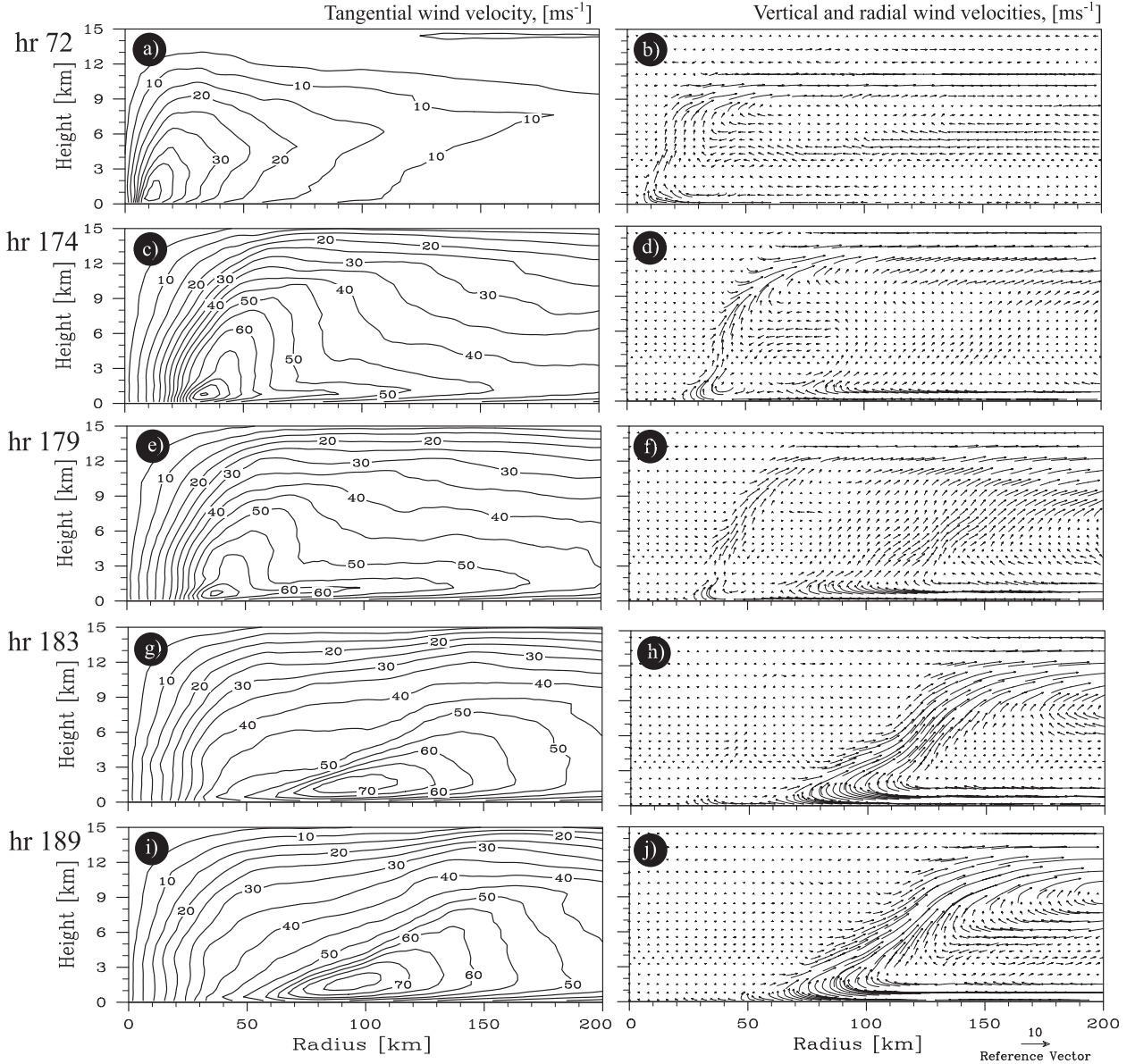


FIG. 1. Radius–height sections of azimuthally averaged (left) tangential (contours) and (right) vertical and radial (vectors) components of the storm-relative wind. Five different integration times are shown, corresponding to hours (a),(b) 72, (c),(d) 174, (e),(f) 179, (g),(h) 183, and (i),(j) 189. Hours 174 and 179 are referred to as hours 18 and 23 in Terwey and Montgomery (2008), Terwey et al. (2013), and Abarca and Montgomery (2013). Note that (a),(b) correspond to about 100 simulation hours before the rest of the panels. Such an early time is presented to contrast the wind field during a time of single-eyewall intensification and during SEF (see text). Note also that (e) corresponds to Fig. 2f in Abarca and Montgomery (2013), except here a snapshot (instead of 2-h average) is shown. Contours are shown every  $5\text{ m s}^{-1}$  and the reference vector magnitude is indicated below (j). The vectors are curved so they are tangential to the represented flow at each point. Note that (c)–(f) are also published as in the top panels of Fig. 2 of Montgomery et al. (2014).

in Bui et al. (2009, their Fig. 2d), with their potential temperature field reaching values lower than  $7^\circ\text{C}$  at the lowest part of their domain. For the case studied herein, the cold anomaly is exacerbated both by the intensity of the simulated storm [maximum azimuthally averaged tangential winds surpassing  $70\text{ m s}^{-1}$ , compared with about  $50\text{ m s}^{-1}$  in Bui et al. (2009)] and

by the broad radial structure of the tangential wind field.<sup>4</sup> The unrealistic cold anomaly is found also by

<sup>4</sup>Observe that in Bui et al. (2009, their Fig. 2b) the  $50\text{ m s}^{-1}$  isolach spans from about 35- to about 45-km radius, while the same isolach roughly spans from 22- to 120-km radius in Fig. 2a.

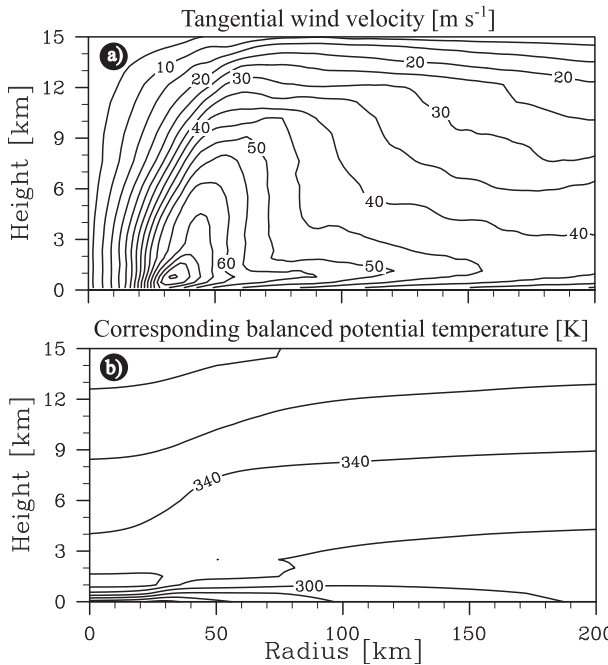


FIG. 2. Radius–height sections of (a) azimuthally averaged tangential component of the storm-relative wind (contours every  $5 \text{ m s}^{-1}$ ) for hour 174 (as in Fig. 1b) and (b) corresponding balanced temperature field (contours every  $10 \text{ K}$ ) calculated as in Smith (2006); see text for details.

Rozoff et al. (2012). Given such an unrealistic cold anomaly, Rozoff et al. (2012) chose to hold the tangential winds constant below 2 km.

The unrealistic cold anomaly in the near-surface potential temperature field in balance with the tangential wind is in stark contrast with the RAMS azimuthally averaged potential temperature in that region ( $32^\circ\text{C}$ ; Fig. 3a). Besides the large cold anomaly at the surface, the balanced temperature field derived using Smith (2006) exhibits static instability in the inner core as a result of the change of sign of the vertical wind shear near the top of the boundary layer and its implications through the thermal wind equation. In contrast, strong changes in the vertical stability are not a characteristic of the azimuthally averaged temperature field (Fig. 3a). It is a useful reminder to note that the unrealistic cold anomaly and vertical stability profiles result from the assumption that the potential temperature field is in balance with the prescribed tangential wind in the boundary layer. Since we aim to assess departures from balance, we will adhere fully to this assumption. While the magnitude of the temperature difference can be thought as a measure of the inappropriateness of the assumption of balance in the boundary layer, it permits the representation of a truly balanced vortex in the Sawyer–Eliassen inversion.

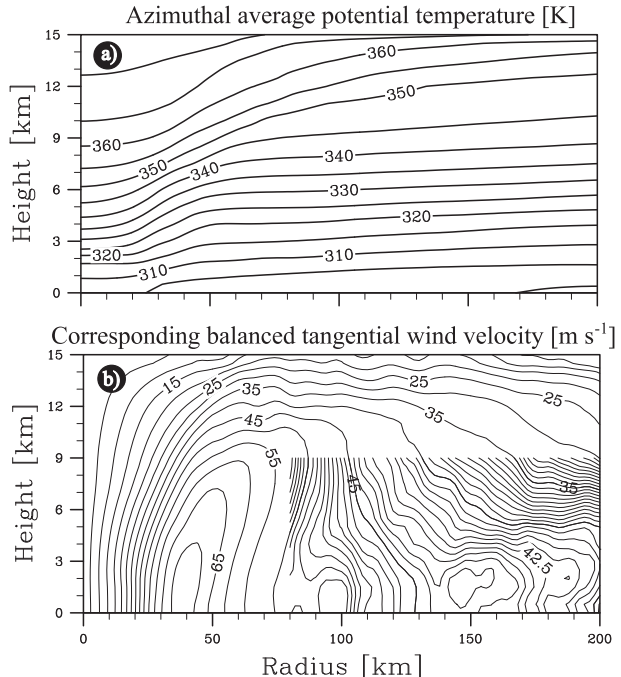


FIG. 3. Radius–height sections of (a) the azimuthally averaged potential temperature for hour 174 and (b) the corresponding balanced tangential wind velocity, calculated as in Holton (2004; see text). Contours are shown every  $5 \text{ m s}^{-1}$  and  $5 \text{ K}$ , except in (b) for radii larger than 80 km and heights lower than 9 km, where contours are shown every  $0.5 \text{ m s}^{-1}$ . Note that (b) is also published as in the left-center panel of Fig. 2 of Montgomery et al. (2014).

Figure 3 shows the azimuthally averaged potential temperature field from the RAMS integration, along with the tangential wind field in balance with the RAMS azimuthally averaged density and pressure fields (not shown). Here, the tangential wind field is computed from the radial pressure gradient force, neglecting the radial-flow component, as is customary in the traditional balance formulation, as described in section 2c(1). In the lower troposphere, there are acute differences between the azimuthally averaged tangential wind and the analogous balanced field. The tangential velocity maximum changes from more than  $80 \text{ m s}^{-1}$  in the average to about  $70 \text{ m s}^{-1}$  in the balanced field (the balanced tangential wind maximum is about 80% of the magnitude of the azimuthally averaged wind maximum), and it is located about 6 km radially outward and 1.5 km above that of the azimuthally averaged maximum. Despite these differences in the velocity maximum, the largest discrepancies between the azimuthal average and the balanced tangential wind field occur radially outward of the radius of maximum winds, in the SEF region. The balanced tangential velocity field Fig. 3b exhibits three discernible tangential wind maxima outside of the primary eyewall. This is in contrast with the RAMS data (Fig. 2a), which

have no tangential wind maximum beyond the primary eyewall at hour 174 and possess just one secondary tangential wind maximum at about 5 h later (Fig. 1g). The three maxima in the balanced tangential wind field are located in the lowest 2.5 km of the model atmosphere, where the differences between the azimuthal average and the corresponding balanced fields are not small.

Just like the stark contrast between the RAMS potential temperature (Fig. 3a) and the balanced potential temperature field (Fig. 2b), the substantial differences between the RAMS tangential wind field (Fig. 2a) and the computed balanced tangential wind field (Fig. 2b) are quantitative indications of the inappropriateness of the assumption that hurricanes are in balance at all heights. The differences are largest in the boundary layer where the tangential wind maximum of the secondary eyewall emerges.

### c. Forcing fields

To integrate the Sawyer–Eliassen model, the diabatic heating rate and tangential momentum forcing functions are required. These functions are computed from azimuthal and 1-h averages of the RAMS integration as described in section 2c(2). Figure 4 shows the forcing functions used in this study. Consistent with the observed secondary circulation (Fig. 1d), Fig. 4a shows that the azimuthally averaged diabatic heating rate exhibits a well-defined maximum confined largely to a vertical column within an annular region about 15 km wide, centered around 40 km and sloping outward. The mean heating rate maximum exhibits a magnitude of about  $70 \text{ K h}^{-1}$ . This value is substantially higher than those previously reported [e.g., about  $20 \text{ K h}^{-1}$  in Bui et al. (2009)]. Both the strong vortex (with tangential wind maximum larger than  $80 \text{ m s}^{-1}$ ) and a highly symmetric structure [Fig. 4 of Terwey and Montgomery (2008)] are factors contributing to this large value. As the primary eyewall begins to weaken around this time, the azimuthally averaged diabatic heating rate decreases substantially reaching values of  $60 \text{ K h}^{-1}$  at hour 179. Figure 4a shows also that as the vortex undergoes SEF, the heat forcing exhibits rates that exceed  $10 \text{ K h}^{-1}$  between 70- and 150-km radius. Figure 4b shows a sink of tangential momentum in a shallow layer above the surface, attributable to the effects of surface friction that, by itself, is acting persistently to decelerate the tangential wind. Not surprisingly, the maximum deceleration is found in the region with the largest tangential wind speeds. The deceleration reaches  $50 \text{ m s}^{-1} \text{ h}^{-1}$  in the region of the primary eyewall and surpasses  $10 \text{ m s}^{-1} \text{ h}^{-1}$  at around 100-km radius. In the middle and upper troposphere, Fig. 4b shows that there is a momentum source radially inwards of the primary eyewall updraft (Fig. 1d) and a momentum sink radially outwards

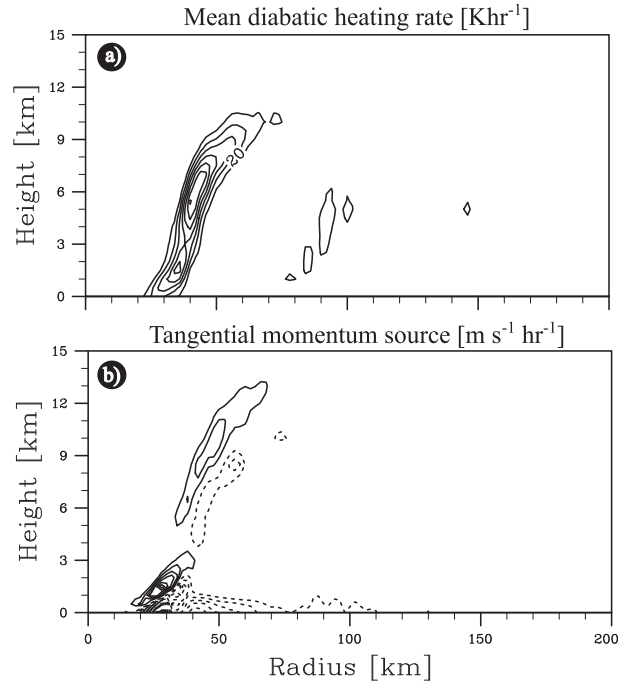


FIG. 4. Radius–height sections of azimuthally averaged forcing functions diagnosed at hour 174 from the three-dimensional RAMS calculation: (a) the heat source (contours every  $10 \text{ K h}^{-1}$ ) and (b) the momentum source (contours every  $10 \text{ m s}^{-1} \text{ h}^{-1}$ ). Negative contours are dashed.

of the same updraft. These sources and sinks are related to eddy momentum fluxes in the eyewall region. While the magnitude of this forcing is large locally (about  $20 \text{ m s}^{-1} \text{ h}^{-1}$ ), it is relatively small compared to the forcing at lower levels, near the surface. As shown below, the effect of this eddy momentum forcing on the overall solution for the mean transverse circulation is relatively small.

### d. RAMS versus Sawyer–Eliassen tangential wind tendency

Figure 5 compares the azimuthally averaged tangential wind tendency and the radial, vertical, and tangential wind velocity of the RAMS integration at hour 174 (left column), with those resulting from the Sawyer–Eliassen model, integrated as described in section 3b, following Smith (2006) (center column) and Holton (2004) (right column). The tangential wind tendency (lowest two rows) is computed as indicated in the figure, as

$$\frac{\partial \bar{v}}{\partial t} = -\bar{u}(\bar{\zeta} + f) - \bar{w} \frac{\partial \bar{v}}{\partial z} \quad (5)$$

for the third row, and as

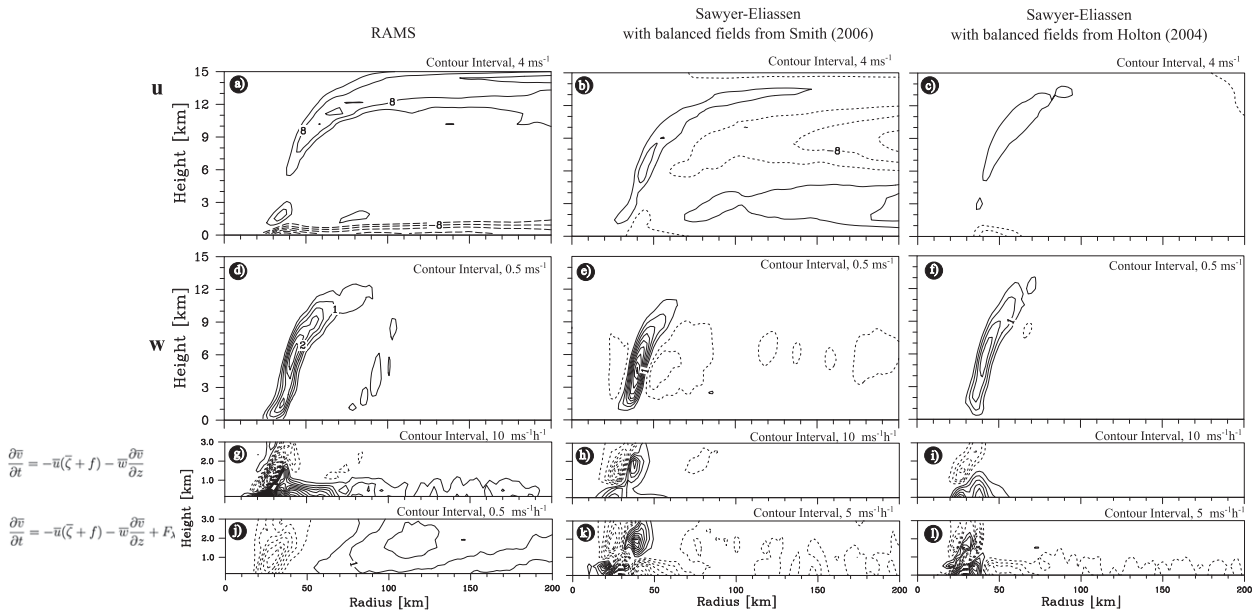


FIG. 5. Vertical cross sections of the (a)–(c) radial and (d)–(f) vertical wind components and (g)–(l) tangential wind tendencies (defined in the equations on the left side of the figure), for (left) the azimuthally averaged fields of the RAMS simulation at hour 174 and for the Sawyer–Eliassen model integrated with balanced fields as in (center) Smith (2006) and (right) Holton (2004). See text for further details and definition of symbols in the equations. Contour intervals are indicated above each panel.

$$\frac{\partial \bar{v}}{\partial t} = -\bar{u}(\bar{\zeta} + f) - \bar{w}\frac{\partial \bar{v}}{\partial z} + F_\lambda \quad (6)$$

for the bottom row. In these two equations, the symbols are as defined before. In the case of the Sawyer–Eliassen model (center and right columns in Fig. 5), we compute the tangential wind tendencies in Eqs. (5) and (6) using the balanced secondary circulation deduced from Eq. (1) instead of the azimuthal averages  $\bar{u}$  and  $\bar{w}$  from the RAMS solution. Note that in the center and right columns in Fig. 5, the difference between the third and bottom row lies with the inclusion of the azimuthally averaged tangential momentum sink.

Figure 5 shows that both the RAMS and the Sawyer–Eliassen results exhibit a secondary circulation typical of a hurricane undergoing SEF, with inflow in the boundary layer and in the midtroposphere, and outflow in the upper troposphere and immediately above the strong inflow in the boundary layer. Figure 5 shows also that while the Sawyer–Eliassen inversions capture the overall secondary circulation structure of the RAMS simulation, there are substantial differences between the RAMS and Sawyer–Eliassen results. As an example, the largest magnitude of vertical motion in the three computations is observed within the primary eyewall (around 40-km radius in the three cases; see Figs. 5d–f), with the balance computation following Smith (2006) exhibiting the largest values (surpassing  $4.5 \text{ m s}^{-1}$ ) and the smallest ( $< 2.5 \text{ m s}^{-1}$ ) in the balance computation following

Holton (2004). The larger upward vertical motion in the balance calculation following Smith (2006) exhibits also larger adjacent subsidence ( $> 1.0 \text{ m s}^{-1}$ ). Such strong subsidence is not observed in the azimuthally averaged RAMS field or in the balance calculation following Holton (2004).

In the region of SEF (between 75- and 150-km radius) the RAMS maximum azimuthally averaged boundary layer inflow surpasses values of  $16 \text{ m s}^{-1}$  (Fig. 5a). In contrast, the Sawyer–Eliassen inversions exhibit much smaller mean-inflow velocities that barely surpass  $4 \text{ m s}^{-1}$  (Fig. 5b) for the case of the Smith (2006) balance methodology and  $3 \text{ m s}^{-1}$  (Fig. 5c) for the case of the Holton (2004) balance methodology. In the same radial region, the vertical motion in the RAMS data exhibits an azimuthal average with magnitude larger than  $0.5 \text{ m s}^{-1}$  (Fig. 5d). The balance calculation computed using the Smith (2006) pathway exhibits also some localized upward vertical motion in the region of SEF that surpasses the  $0.5 \text{ m s}^{-1}$  level (see contours at about 86-km radius and 3-km height in Fig. 5e), unlike the balance calculation computed using the Holton (2004) pathway that does not reach such values.

Figure 5 shows that the differences between the azimuthally averaged radial and vertical RAMS velocity fields and those of the Sawyer–Eliassen model integrations are not of overall structure but of magnitude. The inflow in the boundary layer is substantially underestimated in the Sawyer–Eliassen calculations, by up to

about 80% in the radial region of SEF. The figure shows also that quantitative differences in the secondary circulation translate to quantitative and qualitative differences in tangential wind tendency, with none of the Sawyer–Eliassen results being able to capture even the right sign of the tangential wind tendency in the region of SEF (see appendix B for yet another pathway to characterize the balanced fields consistent with these results). In the radial region of SEF (between about 75- and 150-km radius), the tangential wind tendency, computed from the secondary circulation using the Sawyer–Eliassen integration renders only a modest tangential wind tendency (composed of a weak radial absolute vorticity flux and vertical advection of tangential momentum; see Figs. 5h,i). When the azimuthally averaged momentum sink [Eq. (3)] is added to the foregoing tangential wind tendency computation, based on the secondary circulation of the balance integration, no SEF spinup tendency is predicted. The quantitative differences in inflow result in qualitative differences in tangential wind tendency, since ultimately the tangential wind spinup (in the azimuthally averaged sense) is due largely to the radial flux of absolute vorticity [see Abarca and Montgomery (2013, section 5c, their tangential velocity tendency diagnosis)]. Figure 5 shows that the underestimation of the inflow magnitude, and consequently the underestimation of the absolute vorticity flux, when combined with the vertical advection of tangential momentum, results in spindown in the radial region where SEF is taking place.

The results presented here suggest that during the simulated SEF event, the magnitude of the radial inflow needed to maintain the specified vortices in axisymmetric balance (as defined herein) is much smaller than the inflow generated by latent heating and surface friction in the full-physics simulation. The full-physics simulation includes strong horizontal advective dynamics that arise in the region spanning the transition layer between the surface layer and the nearly inviscid bulk vortex circulation. Because of the strongly coupled nature of the horizontal momentum equations in the composite boundary layer region, the frictional force in the boundary layer results in subgradient winds near the surface, where the radial pressure gradient force is larger than the sum of the centrifugal and Coriolis forces. The subgradient momentum balance near the surface results in an increase of the radial inflow and a correspondingly large radial vorticity flux, the net result of which can be sufficient to generate supergradient flow and tangential wind spinup farther up within the boundary layer. These results suggest that balance dynamics (e.g., Nong and Emanuel 2003; Rozoff et al. 2012) are generally an insufficient theoretical framework to explain secondary eyewall formation.

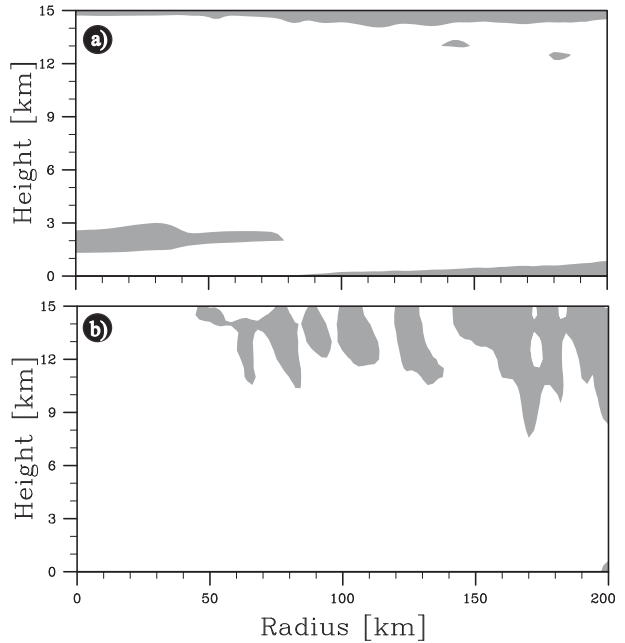


FIG. A1. Radius–height sections of the discriminant  $D$ . Gray shading indicates regions where the ellipticity condition is violated ( $D < 0$ ) for the integrations performed by calculating the balance as in (a) Smith (2006) and (b) Holton (2004).

#### 4. Conclusions

In this study we examine departures from axisymmetric balance dynamics during secondary eyewall formation, in a case of a three-dimensional full-physics integration of a tropical cyclone. The mesoscale simulation is convection permitting, it is integrated in an idealized quiescent environment from a weak mesoscale vortex, and it evolves to develop a canonical eyewall replacement cycle. This study focuses on the time of the simulation during the formation of the secondary eyewall, a few hours before the secondary tangential wind maxima are established.

Departures from axisymmetric balance dynamics are quantified by comparing the secondary circulation and corresponding tangential wind tendency of the mesoscale simulation with those diagnosed after constraining the azimuthally averaged flow to balance dynamics. We refer to balance dynamics as those processes that act to maintain axisymmetric thermal wind balance. In contrast, we refer to unbalanced dynamics as those processes that are related to the axisymmetric portion of the hurricane flow that are not constrained by the thermal wind equation. In our view, unbalanced dynamics include the strong horizontal advective dynamics that arise in hurricanes on account of surface friction and therefore are confined primarily to the low-level region spanning the transition layer between the surface layer and the nearly inviscid

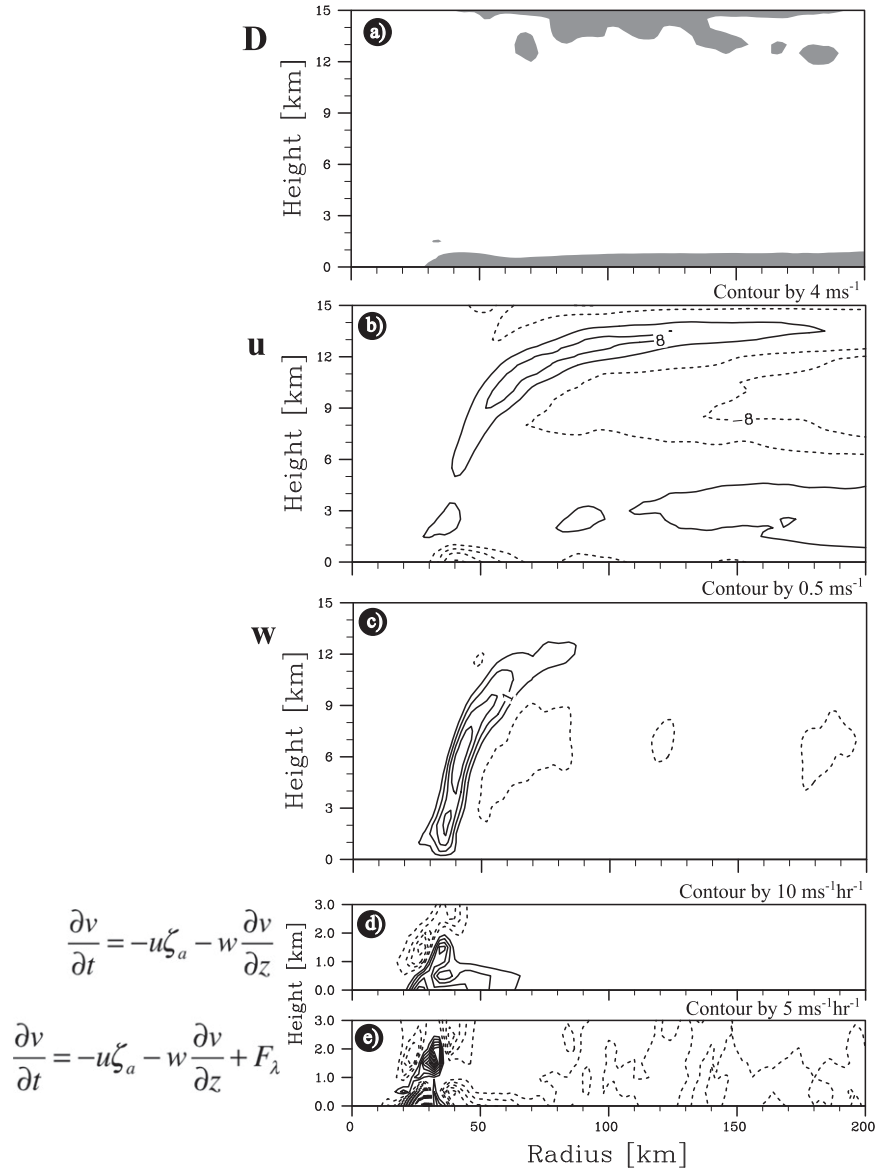


FIG. B1. Radius–height sections of (a) the discriminant, (b) radial and (c) vertical wind components, and (d) and (e) tangential wind tendencies (defined in the equations on the left side of the figure), for the Sawyer–Eliassen model integrated with azimuthally averaged fields (not in balance) from the RAMS simulation at hour 174. See text for details. Contour intervals are indicated above each panel.

bulk vortex circulation. We use the Sawyer–Eliassen balance equation, commonly used as a mean-flow model in the limit of weak departures from circular flow, to diagnose the secondary circulation constrained by axisymmetric balance dynamics. To integrate the Sawyer–Eliassen equation we characterize the background vortex and diagnose the heat and momentum forcing from the mesoscale numerical integration.

Three different ways of characterizing the basic-state vortex in the Sawyer–Eliassen integration are studied. In

one method, we use the azimuthally averaged tangential wind field and compute its corresponding balanced thermodynamical fields, using the thermal wind equation. In a second method, we use the azimuthally averaged pressure and density fields from the mesoscale integration and infer the corresponding balanced tangential velocity field. Finally, as a third method, we characterize the vortex using only azimuthally averaged fields from the mesoscale integration. Azimuthal averages and their analogous estimated balanced fields exhibit many commonalities

throughout the troposphere. However, these fields exhibit large differences in the boundary layer. Such differences are an alternative indication of the inappropriateness of the assumption of axisymmetric balance dynamics (or weak departures therefrom) in the boundary layer.

The most significant finding of this work is that axisymmetric balance dynamics does not capture the tangential wind spinup during secondary eyewall formation. While balance dynamics does capture the overall structure of the secondary circulation of the full-physics simulation, it exhibits quantitative differences that include a large underestimation of inflow in the boundary layer, where the secondary wind maximum emerges. The quantitative underestimation of inflow results in striking qualitative differences in the tangential wind tendency, and balance dynamics are found to be unable to capture, by themselves, the secondary eyewall spinup. These findings are robust to the pathway of balanced vortex characterization for the three different methodologies used in this study.

The results herein offer support to previous studies that point to the importance of unbalanced boundary layer dynamics in secondary eyewall formation. These results suggest that balance dynamics are generally an insufficient theoretical framework to explain secondary eyewall formation. Ongoing analysis that parallels the work presented here is being conducted on other high-resolution numerical simulations carried out using the Weather Research and Forecasting (WRF) Model. The results of this work will be presented in due course.

**Acknowledgments.** The first author gratefully acknowledges the support from the National Research Council (NRC), through its Research Associateship Program, and the host institution, the Naval Postgraduate School (NPS) in Monterey, California. The authors thank Christopher Rozoff and two anonymous reviewers for their substantive comments on the originally submitted manuscript. The work was partially supported by the Office of Naval Research (ONR), through Award N0001412WX20253, and by the National Science Foundation (NSF), through Award ATM-0733380 and IAA-1313948.

## APPENDIX A

### Violation of the Ellipticity Condition

The balanced vortex described in Figs. 2 and 3, forced with the functions in Fig. 4 represents an elliptic problem in most points in the domain. Figure A1 shows the areas where the ellipticity condition is met (white area) and where it is violated (gray area), for the balanced vortex

defined as in Smith (2006) (Fig. A1a) and as in Holton (2004) (Fig. A1b). The two approaches to define balance result in local violations of the ellipticity condition in the upper part of the domain. These violations are related to  $[\xi\chi(\zeta + f) + C\partial\chi/\partial r]$  becoming negative and mostly occur in the region of outflow. The two approaches exhibit also some violations of the ellipticity condition at large radius, near the lower boundary, related to a large  $\partial(\chi C)/\partial z$ . Besides these regions of violation of the ellipticity condition, the computation based on Smith (2006) results also in violations in the lower troposphere near the storm center (between 1- and 3-km heights and for radii less than 80 km) related to  $\partial\chi/\partial z$  becoming positive. The latter violations are related to the vertical instability of the computed balanced temperature field. With the regularization procedure described in section 3, the ellipticity condition is met throughout the domain and the solution of Eq. (1) converges (absolute error smaller than  $10^{-24}$ ) after a few thousand iterations.

## APPENDIX B

### Alternative Vortex Representation

In this appendix we compare the secondary circulation and the corresponding tangential wind tendencies of the RAMS and Sawyer–Eliassen models, using alternative vortex representations. To define the basic-state vortex, the Sawyer–Eliassen equation is integrated using azimuthally averaged dynamical and thermodynamical fields (Figs. 2a and 3a).<sup>B1</sup> The forcing functions employed are those in Fig. 4. With this configuration, the diagnostic balance equation represents an elliptic problem in most points in the domain. Figure B1a shows the areas where the ellipticity condition is met (white area) and where it is violated (gray area). Figure B1a

<sup>B1</sup> Another way of representing the vortex, essentially combining the two methods in the main body of this work, has been considered following a suggestion by D. Nolan (2014, personal communication). This procedure consists of taking the vortex from the second method (Holton 2004; see main text) and computing the thermodynamical fields that would be in thermal wind balance with its wind field (through the first method; Smith 2006; see main text). Strictly speaking, this second iteration is required to ensure consistency between the mass and wind fields using the Holton (2004) methodology. With the second iteration, the corrections to the temperature field are relatively small through most of the vortex, with the largest corrections located in the upper troposphere within approximately 50-km radius from the center of the storm (not shown). With the second iteration, the results from the Sawyer–Eliassen inversion and the derived tangential wind tendency (not shown) are qualitatively and quantitatively very similar to that of the second method (Holton 2004; see main text).

shows that the ellipticity condition is violated locally, at the lower part of the domain. This is related to a large  $\partial(\chi C)/\partial z$ , as described in section 3. With the regularization procedure as described in section 2c(3), the ellipticity condition is met throughout the domain and the solution of Eq. (1) converges (error smaller than  $10^{-24}$ ) after a few thousand iterations.

Figures B1b and B1c show the secondary circulation resulting from the Sawyer–Eliassen integration. These figures show that the spatial structure of the secondary circulation of the corresponding full-physics computation is again broadly captured. The balanced secondary circulation even exhibits a near-surface, secondary inflow maxima that surpasses  $4 \text{ m s}^{-1}$  around 90-km radius. However, the inflow values in the SEF region are much smaller than those in the full-physics integration (cf. Fig. 5a).

Figure B1d shows the tangential wind tendency computed from the Sawyer–Eliassen solution, using only the radial absolute vorticity flux and the vertical advection of tangential momentum. The figure shows modest positive tangential wind tendency in the radial region of SEF (between about 75- and 150-km radius). However, Fig. B1e shows that when the azimuthally averaged momentum sink [Eq. (3)] is added to the tangential wind tendency, no spinup tendency is obtained in the radial region of SEF. That is, quantitative differences in the secondary circulation between the full-physics model (Fig. 5, left column) and the balance diagnostic equation represent striking qualitative differences in storm spinup, as in the results presented in section 3. The foregoing results support the view that axisymmetric balance dynamics as defined herein does not capture the tangential wind spinup during secondary eyewall formation.

## REFERENCES

Abarca, S. F., and K. L. Corbosiero, 2011: Secondary eyewall formation in WRF simulations of Hurricanes Rita and Katrina (2005). *Geophys. Res. Lett.*, **38**, L07802, doi:10.1029/2011GL047015.

—, and M. T. Montgomery, 2013: Essential dynamics of secondary eyewall formation. *J. Atmos. Sci.*, **70**, 3216–3230, doi:10.1175/JAS-D-12-0318.1.

Bell, M. M., and M. T. Montgomery, 2008: Observed structure, evolution, and potential intensity of category 5 Hurricane Isabel (2003) from 12 to 14 September. *Mon. Wea. Rev.*, **136**, 2023–2046, doi:10.1175/2007MWR1858.1.

—, —, and W. C. Lee, 2012: An axisymmetric view of concentric eyewall evolution in Hurricane Rita (2005). *J. Atmos. Sci.*, **69**, 2414–2432, doi:10.1175/JAS-D-11-0167.1.

Bui, H. H., R. K. Smith, M. T. Montgomery, and J. Peng, 2009: Balanced and unbalanced aspects of tropical cyclone intensification. *Quart. J. Roy. Meteor. Soc.*, **135**, 1715–1731, doi:10.1002/qj.502.

Challa, M., and R. L. Pfeffer, 1980: Effects of eddy fluxes of angular momentum on model hurricane development. *J. Atmos. Sci.*, **37**, 1603–1618, doi:10.1175/1520-0469(1980)037<1603:EOEFOA>2.0.CO;2.

Cotton, W. R., and Coauthors, 2002: RAMS 2001: Current status and future directions. *Meteor. Atmos. Phys.*, **82**, 5–29, doi:10.1007/s00703-001-0584-9.

Didlake, A. C., and R. A. Houze, 2011: Kinematics of the secondary eyewall observed in Hurricane Rita (2005). *J. Atmos. Sci.*, **68**, 1620–1636, doi:10.1175/2011JAS3715.1.

Eliassen, A., 1951: Slow thermally or frictionally controlled meridional circulation in a circular vortex. *Astrophys. Norv.*, **5**, 19.

Fang, J., and F. Zhang, 2011: Evolution of multiscale vortices in the development of Hurricane Dolly (2008). *J. Atmos. Sci.*, **68**, 103–122, doi:10.1175/2010JAS3522.1.

Fudeyasu, H., and Y. Wang, 2011: Balanced contribution to the intensification of a tropical cyclone simulated in TCM4: Outer-core spinup process. *J. Atmos. Sci.*, **68**, 430–449, doi:10.1175/2010JAS3523.1.

Hack, J. J., and W. H. Schubert, 1986: Nonlinear response of atmospheric vortices to heating by organized cumulus convection. *J. Atmos. Sci.*, **43**, 1559–1573, doi:10.1175/1520-0469(1986)043<1559:NROAVT>2.0.CO;2.

Harrington, J. Y., 1997: The effects of radiative and microphysical processes on simulated warm and transitional season Arctic stratus. Ph.D. thesis, Colorado State University, 289 pp.

Hawkins, J. D., and M. Helveston, 2004: Tropical cyclone multi-eyewall characteristics. *Preprints, 26th Conf. on Hurricanes and Tropical Meteorology*, Miami, FL, Amer. Meteor. Soc., 276–277.

—, and —, 2008: Tropical cyclone multiple eyewall characteristics. *Extended Abstracts, 28th Conf. on Hurricanes and Tropical Meteorology*, Orlando, FL, Amer. Meteor. Soc., 6B.1.

Hendricks, E. A., M. T. Montgomery, and C. A. Davis, 2004: The role of “vortical” hot towers in the formation of Tropical Cyclone Diana (1984). *J. Atmos. Sci.*, **61**, 1209–1232, doi:10.1175/1520-0469(2004)061<1209:TROVHT>2.0.CO;2.

Hill, G. E., 1974: Factors controlling the size and spacing of cumulus clouds as revealed by numerical experiments. *J. Atmos. Sci.*, **31**, 646–673, doi:10.1175/1520-0469(1974)031<0646:FCTSAS>2.0.CO;2.

Holton, J. R., 2004: *An Introduction to Dynamic Meteorology*. Elsevier Academic, 535 pp.

Houze, R. A. J., S. S. Chen, B. F. Smull, W. C. Lee, and M. M. Bell, 2007: Hurricane intensity and eyewall replacement. *Science*, **315**, 1235–1239, doi:10.1126/science.1135650.

Huang, Y.-H., M. T. Montgomery, and C.-C. Wu, 2012: Concentric eyewall formation in Typhoon Sinlaku (2008). Part II: Axisymmetric dynamical processes. *J. Atmos. Sci.*, **69**, 662–674, doi:10.1175/JAS-D-11-0114.1.

Jordan, C. L., 1958: Mean soundings for the West Indies area. *J. Meteor.*, **15**, 91–97, doi:10.1175/1520-0469(1958)015<0091:MSFTWI>2.0.CO;2.

Judit, F., and S. S. Chen, 2010: Convectively generated potential vorticity in rainbands and formation of the secondary eyewall in Hurricane Rita of 2005. *J. Atmos. Sci.*, **67**, 3581–3599, doi:10.1175/2010JAS3471.1.

Kepert, J. D., 2013: How does the boundary layer contribute to eyewall replacement cycles in axisymmetric tropical cyclones? *J. Atmos. Sci.*, **70**, 2808–2830, doi:10.1175/JAS-D-13-0461.

Kossin, J. P., and M. Sitkowski, 2009: An objective model for identifying secondary eyewall formation in hurricanes. *Mon. Wea. Rev.*, **137**, 876–892, doi:10.1175/2008MWR2701.1.

Kuo, H.-C., L.-Y. Lin, C.-P. Chang, and R. T. Williams, 2004: The formation of concentric vorticity structures in typhoons. *J. Atmos. Sci.*, **61**, 2722–2734, doi:10.1175/JAS3286.1.

—, C.-P. Chang, Y.-T. Yang, and H.-J. Jiang, 2008: Western North Pacific typhoons with concentric eyewalls. *Mon. Wea. Rev.*, **137**, 3758–3770, doi:10.1175/2009MWR2850.1.

Lilly, D. K., 1962: On the numerical simulation of buoyant convection. *Tellus*, **14**, 148–172, doi:10.1111/j.2153-3490.1962.tb00128.x.

Louis, J.-F., 1979: A parametric model of vertical eddy fluxes in the atmosphere. *Bound.-Layer Meteor.*, **17**, 187–202, doi:10.1007/BF00117978.

Maclay, K. S., M. DeMaria, and T. H. Vonder Haar, 2008: Tropical cyclone inner core kinetic energy evolution. *Mon. Wea. Rev.*, **136**, 4882–4898, doi:10.1175/2008MWR2268.1.

Martinez, Y., G. Brunet, and M. K. Yau, 2010a: On the dynamics of two-dimensional hurricane-like concentric rings vortex formation. *J. Atmos. Sci.*, **67**, 3253–3268, doi:10.1175/2010JAS3500.1.

—, —, and —, 2010b: On the dynamics of two-dimensional hurricane-like vortex symmetrization. *J. Atmos. Sci.*, **67**, 3559–3580, doi:10.1175/2010JAS3499.1.

McIntyre, M. E., 2012: Balanced flow. *Encyclopedia of Atmospheric Sciences*, F. Z. G. North and J. Pyle, Eds., Elsevier, 3–20.

Menelaou, K., M. K. Yau, and Y. Martinez, 2012: On the dynamics of the secondary eyewall genesis in Hurricane Willma (2005). *Geophys. Res. Lett.*, **39**, L04801, doi:10.1029/2011GL050699.

Möller, J. D., and M. T. Montgomery, 2000: Tropical cyclone evolution via potential vorticity anomalies in a three-dimensional balance model. *J. Atmos. Sci.*, **57**, 3366–3387, doi:10.1175/1520-0469(2000)057<3366:TCEVPV>2.0.CO;2.

—, and L. J. Shapiro, 2002: Balanced contributions to the intensification of Hurricane Opal as diagnosed from a GFDL model forecast. *Mon. Wea. Rev.*, **130**, 1866–1881, doi:10.1175/1520-0493(2002)130<1866:BCTTIO>2.0.CO;2.

Montgomery, M. T., and L. J. Shapiro, 1995: Generalized Charney–Stern and Fjortoft theorems for rapidly rotating vortices. *J. Atmos. Sci.*, **52**, 1829–1833, doi:10.1175/1520-0469(1995)052<1829:GCAFT>2.0.CO;2.

—, and R. J. Kallenbach, 1997: A theory for vortex Rossby waves and its application to spiral bands and intensity changes in hurricanes. *Quart. J. Roy. Meteor. Soc.*, **123**, 435–465, doi:10.1002/qj.49712353810.

—, M. E. Nicholls, T. A. Cram, and A. B. Saunders, 2006: A vortical hot tower route to tropical cyclogenesis. *J. Atmos. Sci.*, **63**, 355–386, doi:10.1175/JAS3604.1.

—, S. F. Abarca, R. K. Smith, C.-C. Wu, and Y.-H. Huang, 2014: Comments on “How does the boundary layer contribute to eyewall replacement cycles in axisymmetric tropical cyclones?” *J. Atmos. Sci.*, doi:10.1175/JAS-D-13-0286.1, in press.

Nong, S., and K. Emanuel, 2003: A numerical study of the genesis of concentric eyewalls in hurricanes. *Quart. J. Roy. Meteor. Soc.*, **129**, 3323–3338, doi:10.1256/qj.01.132.

Persing, J., M. T. Montgomery, and R. E. Tuleya, 2002: Environmental interactions in the GFDL hurricane model for Hurricane Opal. *Mon. Wea. Rev.*, **130**, 298–317, doi:10.1175/1520-0493(2002)130<0298:EIITGH>2.0.CO;2.

Pfeffer, R. L., and M. Challa, 1981: A numerical study of the role of eddy fluxes of momentum in the development of Atlantic hurricanes. *J. Atmos. Sci.*, **38**, 2393–2398, doi:10.1175/1520-0469(1981)038<2393:ANSOTR>2.0.CO;2.

Pielke, R. A., and Coauthors, 1992: A comprehensive meteorological modeling system—RAMS. *Meteor. Atmos. Phys.*, **49**, 69–91, doi:10.1007/BF01025401.

Press, W. H., S. A. Teukolsky, W. T. Vetterling, and B. P. Flannery, 1992: *Numerical Recipes in C: The Art of Scientific Computing*. Cambridge University Press, 1236 pp.

Qiu, X., and Z.-M. Tan, 2013: The roles of asymmetric inflow forcing induced by outer rainbands in tropical cyclone secondary eyewall formation. *J. Atmos. Sci.*, **70**, 953–974, doi:10.1175/JAS-D-12-084.1.

—, —, and Q. Xiao, 2010: The roles of vortex Rossby waves in hurricane secondary eyewall formation. *Mon. Wea. Rev.*, **138**, 2092–2109, doi:10.1175/2010MWR3161.1.

Rozoff, C. M., D. S. Nolan, J. P. Kossin, F. Zhang, and J. Fang, 2012: The roles of an expanding wind field and inertial stability in tropical cyclone secondary eyewall formation. *J. Atmos. Sci.*, **69**, 2621–2643, doi:10.1175/JAS-D-11-0326.1.

Schubert, W. H., and J. J. Hack, 1982: Inertial stability and tropical cyclone development. *J. Atmos. Sci.*, **39**, 1687–1697, doi:10.1175/1520-0469(1982)039<1687:ISATCD>2.0.CO;2.

—, C. M. Rozoff, J. L. Vigh, B. D. McNoldy, and J. P. Kossin, 2007: On the distribution of subsidence in the hurricane eye. *Quart. J. Roy. Meteor. Soc.*, **133**, 595–605, doi:10.1002/qj.49.

Shapiro, L. J., and H. E. Willoughby, 1982: The response of balanced hurricanes to local sources of heat and momentum. *J. Atmos. Sci.*, **39**, 378–394, doi:10.1175/1520-0469(1982)039<0378:TROBHT>2.0.CO;2.

—, and M. T. Montgomery, 1993: A three-dimensional balance theory for rapidly rotating vortices. *J. Atmos. Sci.*, **50**, 3322–3335, doi:10.1175/1520-0469(1993)050<3322:ATDBTF>2.0.CO;2.

Sitkowski, M., J. P. Kossin, C. M. Rozoff, and J. A. Knaff, 2012: Hurricane eyewall replacement cycle thermodynamics and the relict inner eyewall circulation. *Mon. Wea. Rev.*, **140**, 4035–4045, doi:10.1175/MWR-D-11-00349.1.

Smagorinsky, J. S., 1963: General circulation experiments with the primitive equations. Part I: The basic experiment. *Mon. Wea. Rev.*, **91**, 99–164, doi:10.1175/1520-0493(1963)091<0099:GCEWTP>2.3.CO;2.

Smith, R. K., 2006: Accurate determination of a balanced axisymmetric vortex. *Tellus*, **58**, 98–103, doi:10.1111/j.1600-0870.2006.00149.x.

—, and M. T. Montgomery, 2010: Hurricane boundary-layer theory. *Quart. J. Roy. Meteor. Soc.*, **136**, 1665–1670, doi:10.1002/qj.679.

—, —, and N. Van Sang, 2009: Tropical cyclone spin-up revisited. *Quart. J. Roy. Meteor. Soc.*, **135**, 1321–1335, doi:10.1002/qj.428.

Sun, Y. Q., Y. Jiang, B. Tan, and F. Zhang, 2013: The governing dynamics of the secondary eyewall formation of Typhoon Sinlaku (2008). *J. Atmos. Sci.*, **70**, 3818–3837, doi:10.1175/JAS-D-13-044.1.

Terwey, W. D., and M. T. Montgomery, 2008: Secondary eyewall formation in two idealized, full-physics modeled hurricanes. *J. Geophys. Res.*, **113**, D12112, doi:10.1029/2007JD008897.

—, S. F. Abarca, and M. T. Montgomery, 2013: Comments on “Convectively generated potential vorticity in rainbands and formation of the secondary eyewall in Hurricane Rita of 2005.” *J. Atmos. Sci.*, **70**, 984–988, doi:10.1175/JAS-D-12-030.1.

Walko, R. L., W. R. Cotton, M. P. Myers, and J. L. Harrington, 1995: New RAMS cloud microphysics parameterization. Part I: The single moment scheme. *Atmos. Res.*, **38**, 29–62, doi:10.1016/0169-8095(94)00087-T.

Wang, X., Y. Ma, and N. E. Davidson, 2013: Secondary eyewall formation and eyewall replacement cycles in a simulated hurricane: Effect of the net radial force in the hurricane boundary layer. *J. Atmos. Sci.*, **70**, 1317–1341, doi:10.1175/JAS-D-12-017.1.

Wang, Z., 2012: Thermodynamic aspects of tropical cyclone formation. *J. Atmos. Sci.*, **69**, 2433–2451, doi:10.1175/JAS-D-11-0298.1.

Willoughby, H. E., 1979: Forced secondary circulations in hurricanes. *J. Geophys. Res.*, **84**, 3173–3183, doi:[10.1029/JC084iC06p03173](https://doi.org/10.1029/JC084iC06p03173).

—, 1990: Gradient balance in tropical cyclones. *J. Atmos. Sci.*, **47**, 265–274, doi:[10.1175/1520-0469\(1990\)047<0265:GBITC>2.0.CO;2](https://doi.org/10.1175/1520-0469(1990)047<0265:GBITC>2.0.CO;2).

—, J. A. Clos, and M. G. Shoreibah, 1982: Concentric eye walls, secondary wind maxima, and the evolution of the hurricane vortex. *J. Atmos. Sci.*, **39**, 395–411, doi:[10.1175/1520-0469\(1982\)039<0395:CEWSWM>2.0.CO;2](https://doi.org/10.1175/1520-0469(1982)039<0395:CEWSWM>2.0.CO;2).

Wu, C.-C., Y.-H. Huang, and G.-Y. Lien, 2012: Concentric eyewall formation in Typhoon Sinlaku (2008). Part I: Assimilation of T-PARC data based on the ensemble Kalman filter (EnKF). *Mon. Wea. Rev.*, **140**, 506–527, doi:[10.1175/MWR-D-11-00057.1](https://doi.org/10.1175/MWR-D-11-00057.1).

Yang, Y.-T., H.-C. Kuo, E. A. Hendricks, and M. S. Peng, 2013: Structural and intensity changes of concentric eyewall typhoons in the western North Pacific basin. *Mon. Wea. Rev.*, **70**, 2632–2648, doi:[10.1175/MWR-D-12-00251.1](https://doi.org/10.1175/MWR-D-12-00251.1).

Zhang, D.-L., Y. Liu, and M. K. Yau, 2001: A multi-scale numerical study of Hurricane Andrew (1992). Part IV: Unbalanced flows. *Mon. Wea. Rev.*, **129**, 92–107, doi:[10.1175/1520-0493\(2001\)129<0092:AMNSOH>2.0.CO;2](https://doi.org/10.1175/1520-0493(2001)129<0092:AMNSOH>2.0.CO;2).

Zhou, X., and B. Wang, 2011: Mechanism of concentric eyewall replacement cycles and associated intensity change. *J. Atmos. Sci.*, **68**, 972–988, doi:[10.1175/2011JAS3575.1](https://doi.org/10.1175/2011JAS3575.1).

—, —, X. Ge, and T. Li, 2011: Impact of secondary eyewall heating on tropical cyclone intensity change. *J. Atmos. Sci.*, **68**, 450–456, doi:[10.1175/2010JAS3624.1](https://doi.org/10.1175/2010JAS3624.1).